SOFC Durability against Standby and Shutdown Cycling

M. Hanasaki,[a] C. Uryu,[a] T. Daio,[b] T. Kawabata,[b] Y. Tachikawa,[c] S. M. Lyth,[c,*] Y. Shiratori,[a,b,c,d] S. Taniguchi,[b,d] and K. Sasaki[a,b,c,d,*,z]

[a]*Faculty of Engineering, Kyushu University, Nishi-ku, Fukuoka 819-0395, Japan*
[b]*International Research Center for Hydrogen Energy, Kyushu University, Nishi-ku, Fukuoka 819-0395, Japan*
[c]*International Institute for Carbon-Neutral Energy Research (WPI-I2CNER), Kyushu University, Nishi-ku, Fukuoka 819-0395, Japan*
[d]*Next-Generation Fuel Cell Research Center (NEXT-FC), Kyushu University, Nishi-ku, Fukuoka 819-0395, Japan*

To simulate realistic operating conditions in SOFC systems, we investigate the influence of thermal cycling on the performance of electrolyte-supported planar SOFCs. Thermal cycling is often associated with interruption of fuel supply, with three main modes; hot standby, cold standby, and shutdown. Cell performance degradation is most significant during shutdown cycles. Nickel oxidation and agglomeration are more pronounced when SOFCs are subjected to lower temperatures for longer periods of time, leading to significant performance degradation. Ostwald ripening at the anode leads to degradation as Ni grains increase in size with cycling. Ni particle precipitation on the anode zirconia grains and along electrolyte grain boundaries is found for the first time in shutdown cycling tests. When H_2S is mixed with the fuel, the internal reforming reactions and electrode reactions are inhibited by sulfur poisoning of the Ni anodes, accelerating degradation. The SOFC cycling degradation mechanisms are discussed in detail.
 [DOI: 10.1149/2.0421409jes]

Manuscript submitted February 24, 2014; revised manuscript received May 21, 2014. Published June 5, 2014.

Solid oxide fuel cells (SOFCs) have several advantages including high efficiency, fuel flexibility, and utilization of non-noble metal, Pt-free catalysts, due to their relatively high operation temperature. Commercialization of SOFC systems for residential electric power applications began in Japan in 2011. Such systems are frequently stopped and restarted in normal operation, e.g. when power is not required, or in an emergency. Such start-stop operation results in thermal cycling, and is often associated with an interruption in fuel supply. Although it is well known that thermal and redox cycling under start-stop operation deteriorates SOFC electrochemical performance,[1–15] there are only a limited number of studies that systematically focus on this technologically relevant issue.

Continuous SOFC stack operation with constant power output generally results in a gradual degradation in performance during long-term operation (SOFCs should run for up to a decade). However, SOFCs can suffer to a greater degree from *changes* in operation conditions. Due to thermal expansion mismatch between the different components, the cells can suffer from mechanical degradation mechanisms, such as delamination and crack formation with simple thermal cycling. Changes in atmosphere can result in more serious degradation. The influences of thermal cycling and current density cycling on cell degradation have been previously investigated.[1–4] The change in volume causes Ni agglomeration.[5–7] Redox cycles are typically associated with oxidation of Ni particles at the anode.[8–12] Furthermore, redox cycling results in the formation of Ni hydroxides at a certain vapor pressure in oxidizing atmosphere, with a high water vapor concentration.[13,14] In real residential SOFC power units, cells and stacks are not subjected to these different conditions independently; the changes occur much more dynamically. Therefore, cycle durability studies should be performed using realistic operation protocols that simulate typical operational conditions. To the best of our knowledge, SOFC cycle durability has not been studied using such realistic protocols thus far.

Here, we explore the influence of thermal cycling on SOFC cell performance using three different protocols; hot standby, cold standby, and shutdown. These are investigated by varying the number of thermal cycles, cooling rate, and fuel composition. The aim of this study is to systematically clarify the SOFC degradation mechanisms caused by realistic start-stop cycle operations.

*Electrochemical Society Active Member.
zE-mail: sasaki@mech.kyushu-u.ac.jp

Experimental

Cell preparation and characterization.— Figure 1a shows a schematic of the SOFC single button cell used in this study. Scandia-stabilized zirconia (ScSZ) plates (10 mol% Sc_2O_3,1 mol% CeO_2, 89 mol% ZrO_2, Daiichi Kigenso Kagaku Kogyo Co., Ltd., Suminoe-ku, Osaka, Japan) with a diameter of 20 mm and a thickness of 200 μm were used as solid electrolytes. Anode powders were prepared by mixing NiO (>99.9%, Kanto Chemical, Japan) and ScSZ in ethanol, ball milling for 24 h, and subsequent drying. Anode paste was prepared by blending the anode powders with organic binder (α-terpineol) and homogenization using three-roller grinding mills (Exakt, Germany). Anode layers were screen-printed on the ScSZ electrolyte, followed by sintering in air at 1300°C for 3 h. The anode consisted of 2 layers; the weight ratio of the first layer (the electrochemical functional layer) was NiO:ScSZ = 56:44. The second layer (for current collection) had a weight ratio of NiO:ScSZ = 80:20.

The first cathode layer comprised of $(La_{0.8}Sr_{0.2})_{0.98}MnO_3$ (LSM, >99.9%, Praxair, USA) and ScSZ powders in a weight ratio of 1:1, deposited on the electrolyte. The second layer comprised of LSM powder calcined in air at 1400°C for 5 h. Cathode layers were screen-printed on the counter side of the ScSZ electrolyte plate, followed by sintering in air at 1200°C for 5 h. Figure 1a shows the thickness of each layer after sintering.

Pt paste (U-3401, N. E. Chemcat, Japan) was painted with a geometric area of ca. 0.04 cm^2 near the edge of the cathode, and used as a reference electrode (RE). The distance between the edge of the cathode and the reference electrode was adjusted to be greater than 0.6 mm, in order to detect potentials within the electrolyte pellet. It should be noted that the potential of the RE could be shifted relative to the potential in the middle of the electrolyte plates in between the electrodes, which can affect the values obtained for the ohmic loss.[16,17] Since the anode potential was measured between the anode and the reference electrode at the cathode side, it has a higher value than the cell voltage by the potential difference between the cathode and the reference electrode. Pt mesh (80 mesh acting) was attached to each electrode surface as a current collector. The thickness and geometric area of the electrode layers were approximately 60 μm and 8 × 8 mm^2 (0.64 cm^2), respectively.

Figure 1b shows the SOFC structure, including glass rings, alumina rings, and alumina-based ceramic seals (AronCeramic D-type, ToaGosei Co., Ltd, Tokyo Japan). The Pyrex glass rings used here have an inner diameter of 16 mm and an outer diameter of 20 mm,

(a)

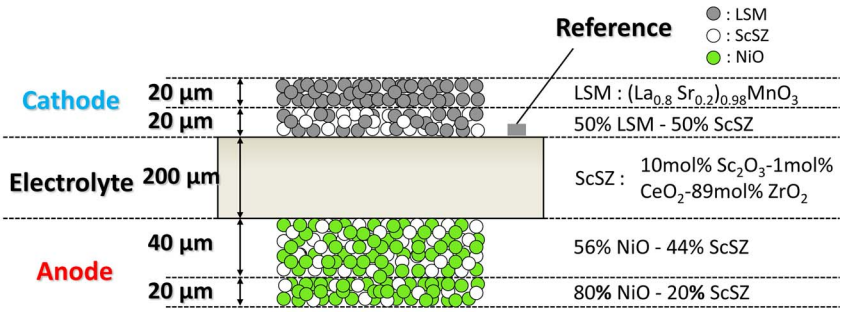

(b)

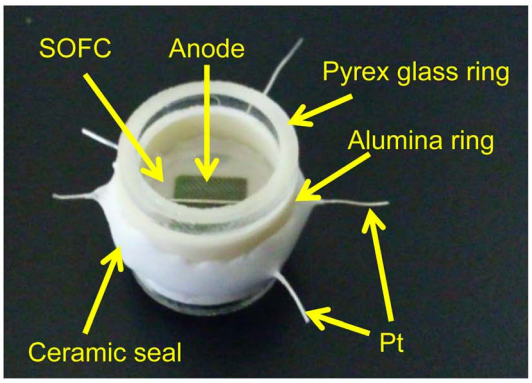

(c)

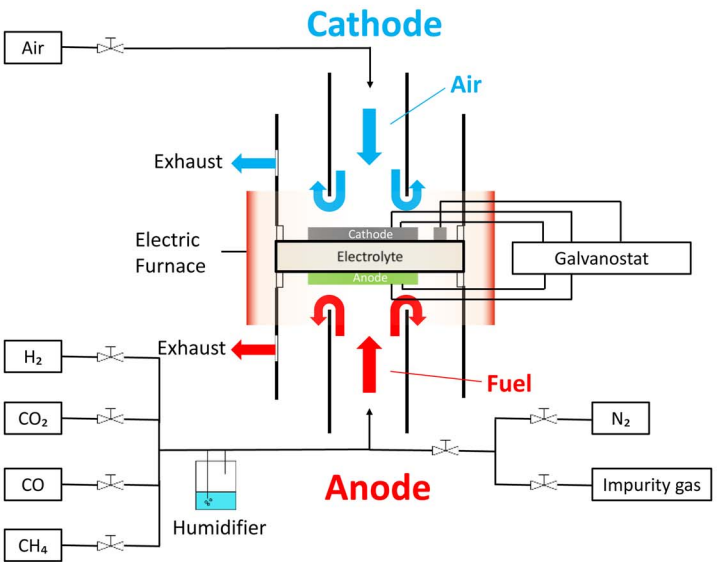

Figure 1. (a) Schematic of the SOFC model single cell (with reference electrode). Given thicknesses are post-sintering. (b) Photo of the glass-sealed cell before heat-treatment at 1000°C. (c) Electrochemical setup.

with a thickness of 3 mm. They are composed of SiO_2 (80.7 wt%), B_2O_3 (12.9 wt%), Na_2O (3.8 wt%), Al_2O_3 (2.2 wt%), and K_2O (0.4 wt%). Figure 1c shows the electrochemical experimental setup. Before measuring the electrochemical characteristics, the cell was heated at a rate of 200°C h^{-1} to 1000°C, in order to melt the Pyrex glass rings (see Fig. 1b). After melting, the alumina rings, ceramic seal, and alumina tubes were all connected and the cell was effectively sealed. 3% humidified H_2 gas was subsequently supplied to the anode with a flow rate of 100 mL/min, at 1000°C for 1 h, in order to reduce the NiO to Ni metal. The cell was then cooled to 800°C. Cell performance (i.e. I-V characteristics, non-ohmic overvoltages, and ohmic losses) was measured at 800°C, utilizing three different types of fuel gas; (a) 3% humidified H_2, (b) 50% pre-reformed CH_4, and (c) 50% pre-reformed CH_4 with 5 ppm H_2S. The 50% pre-reformed CH_4 gas used in this study simulates the partially reformed methane-based gas typically used in residential SOFC systems. By utilizing this fuel, the electrical efficiency can be improved by (partial) internal reforming, whilst preventing sharp temperature decrease near the entrance of SOFC cell stacks by endothermic internal reforming reactions. The 50% pre-reformed CH_4 used here comprises 33 mL/min H_2, 7 mL/min CO, 10 mL/min CH_4, and 3 mL/min CO_2.

Thermal cycling tests were conducted according to three protocols. Changes in cell performance were measured at 0.2 Acm^{-2}. A field-emission scanning electron microscope, coupled with energy-dispersive X-ray analysis (FESEM-EDX, Hitachi High-Technologies, S-5200, EDAX genesis 4000 / JSM-700IF JEOL, Japan, INCA Energy 4.0, Oxford Instruments Analytical, UK) and a focused-ion beam system coupled with SEM (FIB-SEM HeliosNanolab 600i, FEI, USA)

were applied to investigate changes in the anode microstructure and chemical composition after cycling tests. Sample treatment by FIB was performed with an acceleration voltage of 30 kV, a current density of 9.4 nA, and a slice-pitch of 100 nm. SEM-EDX observation in FIB-SEM was made with an acceleration voltage of 10 kV with voxels of 256 by 200 for 3-dimentional EDX mapping of Ni and Zr. One voxel was 496 × 496 × 100 nm^3.

Chemical compositions in thermochemical equilibrium were derived using thermochemical calculation software (HSC Chemistry, Version 7.1. Outokumpu Research Oy, Finland). This software gives the vapor pressures of various compounds in equilibrium using the Gibbs energy minimization procedure.

Durability cycle protocols.— Conditions in practical SOFC systems are simulated using three different protocols; (1) hot standby, (2) cold standby, and (3) shutdown. Details of each cycle protocol are shown in Fig. 2.

During short time periods where power is not required (e.g. at night), residential SOFC systems are cooled down to around 600°C, and a small amount of electricity is continuously generated to maintain minimum required system operation. The hot standby protocol (Fig. 2a) simulates such conditions. Cells are cooled down to 600°C at a rate of 400°C h^{-1}, kept at 600°C for 30 min, heated to 800°C at a rate of 400°C h^{-1}, and then kept at 800°C for 1 h. No interruption in fuel supply occurs during the hot standby protocol.

The cold-standby protocol simulates longer-term shutdown conditions, e.g. when the user is absent for extended periods of time. In this situation, the system is stopped in a controlled manner, and cooled down naturally. In the cold-standby protocol, a single cell is cooled down to 200°C at 100°C h^{-1}, kept at 200°C for 1 h, heated to 800°C at 100°C h^{-1}, and then maintained at 800°C for 1 h. Fuel gas is supplied during power generation at 800°C, whilst diluted H_2 (5% H_2 / 95% N_2) is supplied during the cooling and heating steps.

The shutdown protocol simulates emergency shutdown, e.g. during a blackout, or in an earthquake. In this situation, the fuel supply shuts off, and the temperature changes very quickly. In the shutdown protocol, the cell is cooled down to 400°C at three different rates; 400°C h^{-1} (over 1 h), 200°C h^{-1} (over 2 h), or 100°C h^{-1} (over 4 h), and then maintained at 400°C for 30 min. The cell is then heated to 800°C at 400°C h^{-1}, and kept at 800°C for 1 h. Fuel is supplied during heating and power generation. However, the fuel supply is stopped during cooling and at the lowest temperature. After each cycle, the temperature is maintained at 800°C, and the cell voltage is measured at constant current density (0.2 Acm^{-2}).

Degradation During Different Cycle Protocols

The electrochemical performance of the model cells was evaluated using 3%-humidified H_2 fuel in hot standby, cold standby, and shutdown modes. Ten thermal cycles were applied for each protocol. The resulting change in cell voltage is shown in Fig. 3. Very little degradation occurs during the hot standby protocol. However, performance degradation is more pronounced in the shutdown and cold standby tests. In the cold standby test, diluted H_2 is supplied when the cell is cooled and heated, such that Ni is not easily oxidized. However, the network of zirconia grains in the anode (which normally prevents Ni agglomeration) can change due to thermal expansion mismatch, leading to agglomeration of Ni and an associated disruption of the electronic conduction pathways, resulting in an increase in ohmic losses. The shutdown protocol results in the most serious degradation (Fig. 3). For widespread commercialization of SOFCs, it is essential to understand the degradation mechanisms under emergency shutdown conditions. Therefore, herein we focus on the shutdown situations. Degradation phenomena in the shutdown protocol are evaluated by varying; (i) the number of cycles, (ii) the cool-down rate, and (iii) the type of fuel.

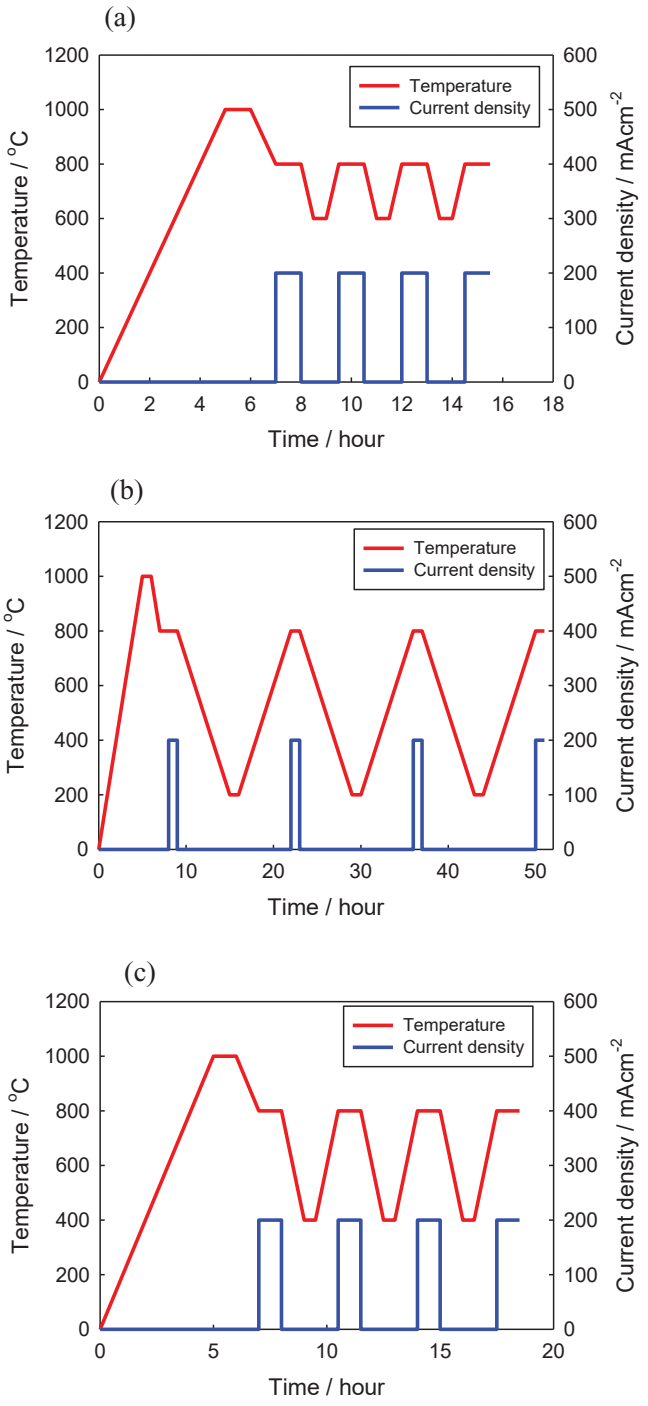

Figure 2. (a) Hot standby; (b) cold standby; and (c) shutdown cycle protocols.

Degradation During the Shutdown Protocol

Dependence on the number of cycles.— The dependence of electrochemical performance on the number of cycles was examined using 3%-humidified H_2 fuel. The change in cell voltage and anode potential over 50 shutdown cycles is shown in Fig. 4a. The change in anode-side IR loss, anodic polarization, cathode-side IR loss, and cathodic polarization are shown in Fig. 4b, deconvoluted using the reference electrode and the current-interrupt technique. Figure 4 indicates that anode-side voltage losses are responsible for the main component of degradation, suggesting that the anode suffers from damage with thermal cycling. During shutdown tests, the fuel supply was stopped during cooling, such that reducing conditions are not

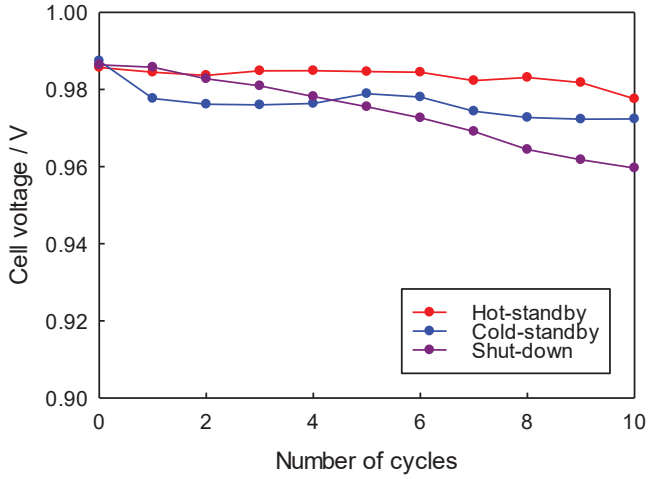

Figure 3. Cell voltage during 10-cycle durability tests at 0.2 Acm^{-2}, using 3%-humidified H_2 fuel: Hot standby; cold standby; and shutdown (with a cooling rate of 400°C h^{-1}).

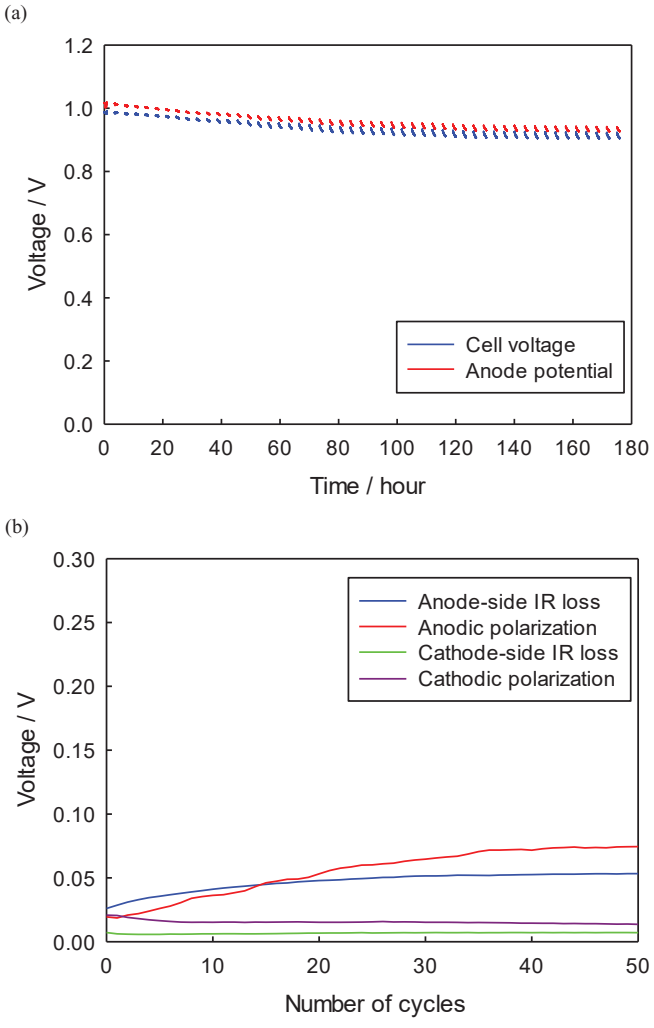

Figure 4. (a) Cell voltage and anode potential (vs. RE, in air). (b) Breakdown of voltage losses at 0.2 Acm^{-2} during a 50-cycle shutdown durability test with 3%-humidified H_2 fuel (cool-down rate: 400°C h^{-1}). Since the anode potential was measured as the voltage between the anode and the reference electrode on the cathode side (in air), the anode potential gives a higher value than the cell voltage by an amount corresponding to the cathode-side voltage losses.

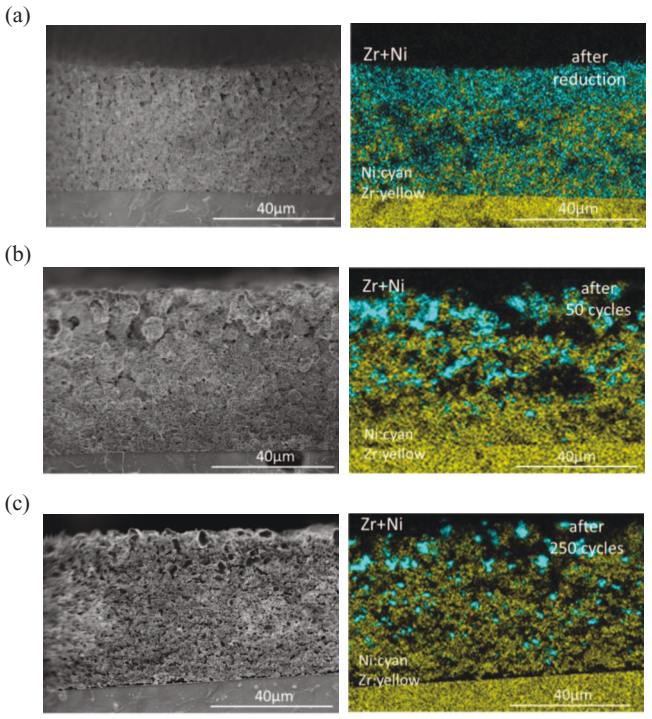

Figure 5. FESEM micrographs and EDX elemental mapping of the Ni-ScSZ cermet anode; (a) after the initial reduction treatment, and then after shutdown durability tests with 3% humidified H_2 fuel (cool-down rate: 400°C h^{-1}) with (b) 50 cycles, and (c) 250 cycles. Note that, since the fracture surface of the anode layer was analyzed, hollow portions of the anode cross-section exhibited weak EDX signals and thus dark contrast.

necessarily maintained. Additionally, the cell, alumina tube, and glass seals could crack at lower temperatures due to thermal expansion mismatch, allowing ambient air into the anode compartment, and leading to oxidation of Ni at the anode. The volume change of Ni grains caused by repeated redox cycling could lead to destruction of the conductive network.[5] Consequently, cell performance degradation in the shutdown protocol is assumed to be associated with changes in anode microstructure.

In order to confirm this change in anode microstructure, FESEM coupled with EDX was performed. Figure 5 shows the anode cross-section after durability testing. A decrease in the amount of Ni near the anode triple-phase-boundary (TPB) is observed with cycling, along with Ni grain coarsening near the anode surface. In addition, EDX analysis reveals that the Ni/Zr ratio (across the whole anode cross-section) falls from 0.68 to 0.19 after the 50-cycle test, clearly indicating the loss of Ni. This leads to a decrease in the number of electrochemical reaction sites, and consequent cell performance degradation as the number of shutdown cycles increases.

The change in Ni distribution may be due to Ostwald ripening. To verify this, we conducted 50-cycle durability tests for two different anode compositions; a bilayer anode with different grain sizes (as in Fig. 1a), and a monolayer anode with homogeneous grain size. Figure 5b and Fig. 6 show FESEM micrographs coupled with EDX elemental mapping of the anode cross-section of the cells after the 50-cycle durability tests. For the bilayer anode (case (i)), a decrease in the amount of Ni around the anode triple-phase boundary, and consequent Ni grain coarsening around the anode surface are clearly observed. However, in case (ii) (as shown in Fig. 6), the Ni grains are homogeneously distributed even after 50 cycles. In this study, we used cells with a high ratio of Ni in the anode current collecting layer to improve in-plane electronic conductivity, as in Fig. 1a. Ostwald ripening occurs due to the difference in Ni grain size, leading to structural change in the anode layer. This result clearly suggests that

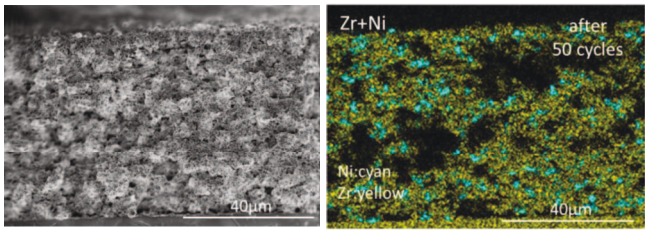

Figure 6. FESEM micrographs and EDX elemental mapping of a Ni-ScSZ cermet anode with monolayer anode composition, after 50 cycles of a shut-down durability test (cool-down rate: 400°C h^{-1}, 3%-humidified H_2 fuel). Note that, since the fracture surface of the anode layer was analyzed, hollow portions of the anode cross-section exhibited weak EDX signals and thus dark contrast.

homogeneous distribution of Ni grain size can inhibit such degradation phenomena caused by Ostwald ripening.

Figure 7 shows the equilibrium compositions of the Ni-O-H system in humidified H_2, calculated thermo-chemically between 400 and 1000°C. $Ni(OH)_2$ *(g)* can exist at around 800°C. In addition, comparing the results for (a) 3%-humidified H_2 and (b) 90%-humidified H_2 (Fig. 7), it is observed that there is a higher $Ni(OH)_2$ *(g)* vapor pressure at higher water vapor concentration. Water vapor forms around triple-phase boundaries by anode reactions. In the shutdown protocol, the fuel supply is stopped during cooling. As a result, the amount of water vapor near the anode is relatively high, since water vapor still remains in the anode chamber. Furthermore, hydrogen may escape, or ambient air may flow into the anode chamber and react with residual H_2 to form additional water vapor (due to cracked seals), resulting

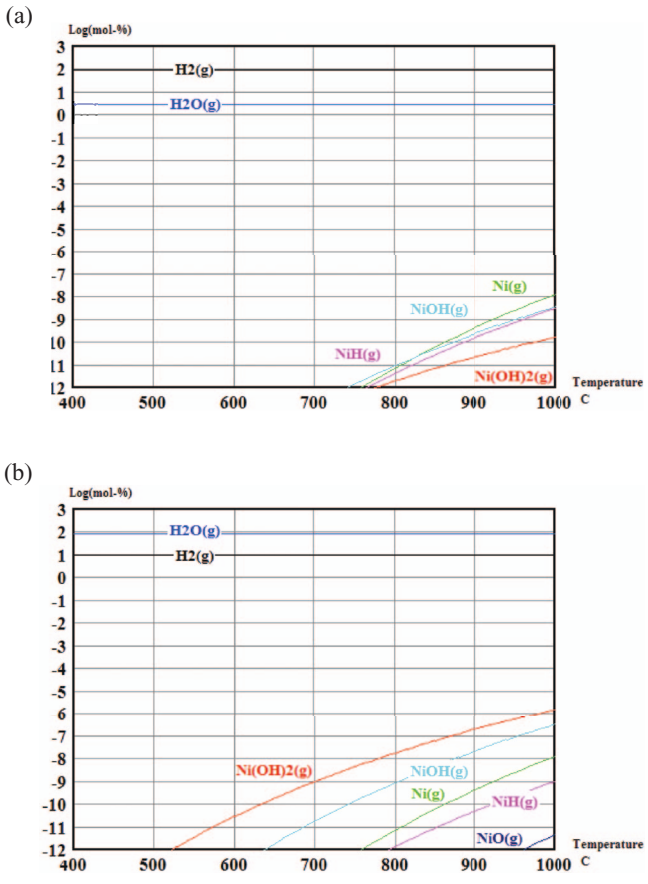

Figure 7. Thermochemically calculated equilibrium compositions of the Ni-O-H system in (a) 3%-humidified H_2, and (b) 90%-humidified H_2 between 400 and 1000°C.

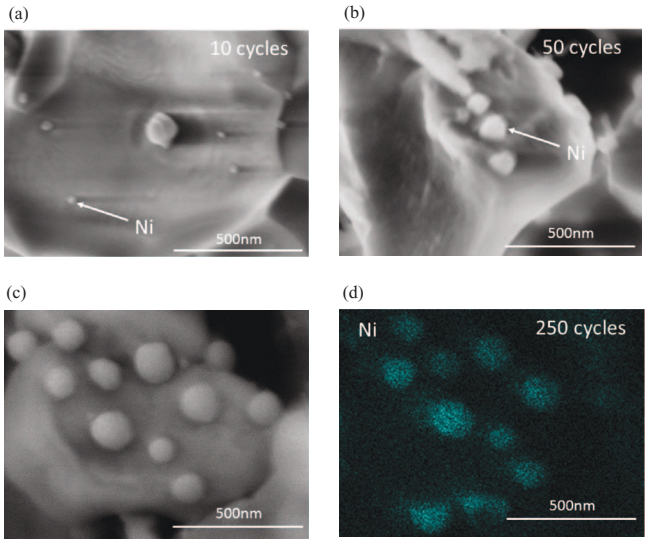

Figure 8. FESEM micrographs of Ni particles on anode zirconia grains after shutdown cycle durability tests (cool-down rate: 400°C h^{-1}, 3%-humidified H_2 fuel) after; (a) 10 cycles, (b) 50 cycles, and (c) 250 cycles. (d) EDX elemental mapping after 250 cycles. Such Ni precipitates were mainly observed in the anode layer, near the electrolyte interface.

in a further increase in oxygen partial pressure. Higher water vapor pressure (i.e. higher oxygen partial pressure) leads to an increase in $Ni(OH)_2$ *(g)* vapor pressure and thus a decrease in the amount of Ni. As expected from Fig. 7, the vapor pressure of $Ni(OH)_2$ *(g)* decreases with decreasing temperature during thermal cycling, and thus Ni particles precipitate at lower temperatures. $Ni(OH)_2$ *(g)* tends to be absorbed on larger Ni particles due to Ostwald ripening, such that the larger Ni particles around the anode surfaces grow even larger, and the smaller Ni particles around the anode triple-phase boundary decrease in size.

By repeating these evaporation and precipitation processes, Ni particles deposited on zirconia grains also increase in size. Ni particle precipitation on the zirconia grain surfaces in the anode layer is clearly observed in Fig. 8. These micrographs confirm that Ni particles are precipitated via the gas phase, and that these precipitated Ni particles increase in size with cycling. Such Ni precipitates were observed in the anode layer near the electrolyte, but not to the same extent near the surface of the anode layer. This result indicates that the Ni-based vapor phase forms near the triple-phase boundary, and precipitates within the porous anode layer. Such Ni particle precipitation on zirconia grains has also been reported in chlorine poisoning of a Ni-based cermet anode.[18]

The decrease in the amount of Ni near the triple-phase boundary results in a decrease in the electrochemical activity due to the loss of electrochemical reaction sites with cycling. The increase in anode Ni grain size and the number of isolated Ni particles on the zirconia grains leads to cell performance degradation.

Dependence on the cooling rate.— The electrochemical performance of the model cells was investigated for the shutdown protocol using 3%-humidified H_2 fuel, and two different cool-down rates of (a) 200°C h^{-1}, and (b) 100°C h^{-1}. These correspond to a period of time in shut-down mode of 2 h and 4 h, respectively. The cell voltage, and analysis of the voltage losses are shown in Fig. 9. The durability test was made over 250 cycles for case (a,c), but only for 74 cycles in case (b,d).

Figure 9 indicates that the anode-side losses (in particular the anode-side IR loss), and the degradation rates increase for slower cool down rates. Since the fuel supply is completely shut off during cooling, a longer time spent cooling the device results in a longer period of fuel starvation at lower temperature. Consequently, the cells are

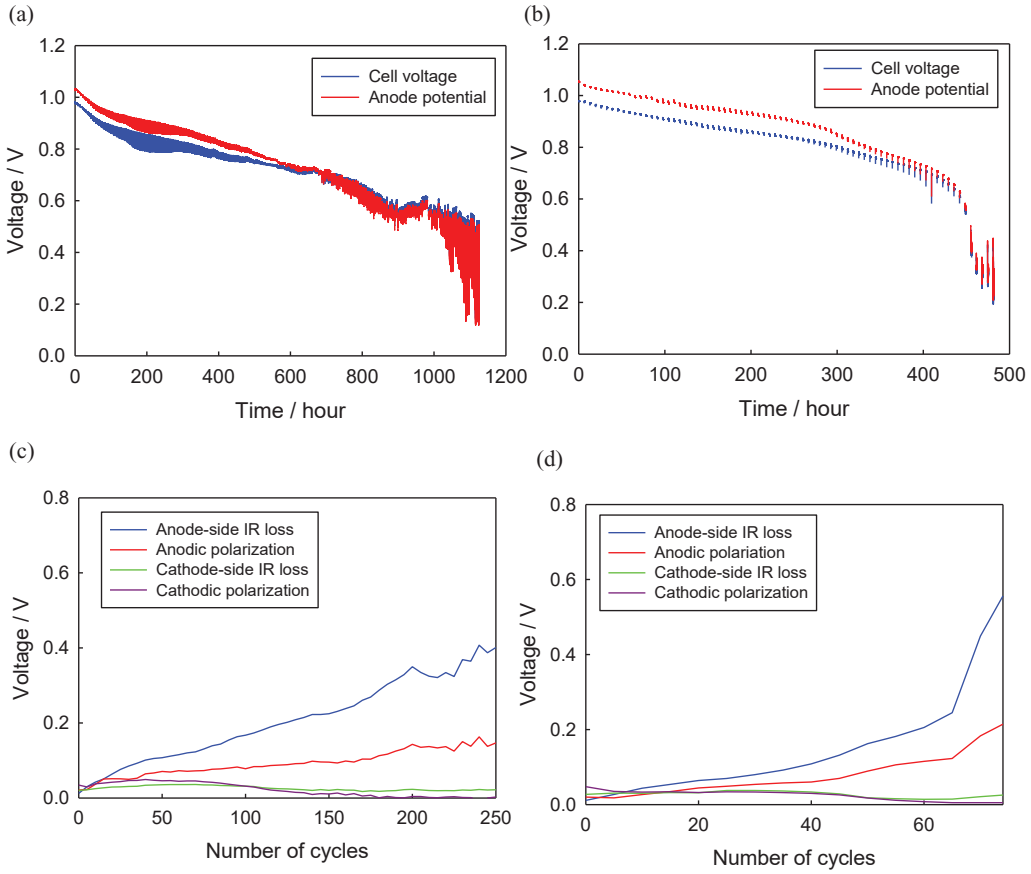

Figure 9. (a,b) Cell voltage and anode potential and (c,d) voltage losses (ohmic loss and non-ohmic polarization both at the anode and the cathode) at 0.2 Acm^{-2} (vs. RE, in air) during the 250 cycle shut down durability tests (3%-humidified H_2 fuel), with different cool down rates; (a,c) 200°C h^{-1} (over 2 h) and (b,d) 100°C h^{-1} (over 4 h). In case (b,d), the cycle test was stopped at 74 cycles since no cell voltage was generated at this current density at that point.

exposed to oxidizing atmosphere for a longer period of time. Repeated oxidation/reduction cycles under these conditions for the Ni anodes lead to cell performance degradation. Insufficient sealing further promotes oxidation of Ni at the anode during cooling. A combination of these effects results in the most serious cell degradation when the cell is in shut-down mode for 4 h. The cell shown in Figs. 9b and 9d did not generate any power after 74 cycles at 0.2 Acm^{-2}.

The open circuit voltage (OCV) was also measured before and after various cycle tests. The average OCV for the 3%-humidified H_2 fuel was 1.070 ± 0.005 V at 800°C, measured in more than 10 different cells before and after cycle tests, so that gas leakage can be considered to be negligible at 800°C. During the most severe shutdown test with 4 h spent in shut-down mode, the OCV at 800°C showed very little variation from an initial value of 1.068 V; to 1.061 V after 25 cycles; 1.062 V after 50 cycles; and 1.060 V after 74 cycles. However, even at 800°C, the OCV began to decrease immediately after stopping the fuel supply, and approached zero after around 10 min. This suggests that slight leakage may occur during severe cycling, and that imperfect sealing causes a gradual increase in the oxygen partial pressure on the anode side, after stopping the fuel supply. A continuous supply of H_2-containing fuel and/or substitution with inert gas such as N_2 may therefore be essential to completely prevent anode Ni oxidation during cycling.

Figure 10 shows FESEM and FIB-SEM micrographs of the anode cross-section of a degraded cell after reduction treatment at 800°C for 1 h (with fuel supply), followed by cooling in nitrogen, after the 74-cycle durability test. Many large, isolated Ni particles are observed with a diameter of ~10 μm, throughout the anode layer (Fig. 10a). Large, >5 μm Ni grains are identified by EDX, with a submicron-scale mesoporous structure. This is as a result of the reduction of NiO to metallic Ni, which is accompanied by large volume shrinkage. Such mesoporous structures are formed during repeated redox cycling, which accelerates sintering within the anode layer.

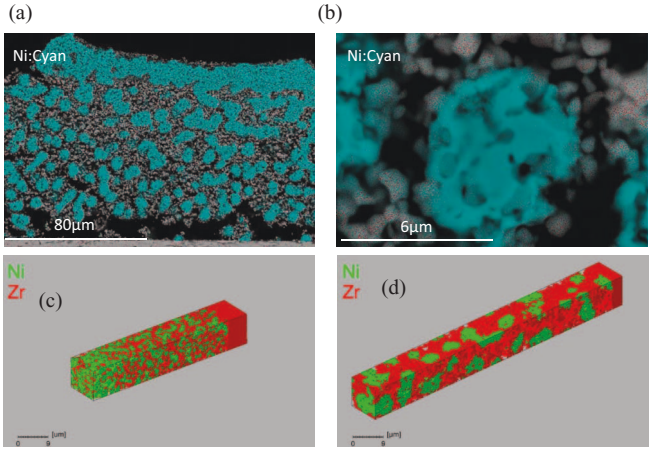

Figure 10. FESEM micrograph overlaid with EDX elemental mapping of Ni grains in the anode after 74 shutdown durability cycles (cool down rate: 100°C h^{-1}, 3%-humidified H_2 fuel). (a) shows the whole anode layer, and (b) shows a typical Ni particle at higher magnification. 3D reconstructed FIB-SEM micrographs of the Ni-ScSZ cermet anode; (c) just after the initial reduction treatment, and (d) after the 74-cycle durability test. In both cases, the electrolyte is at the top right, and the anode is at the lower left.

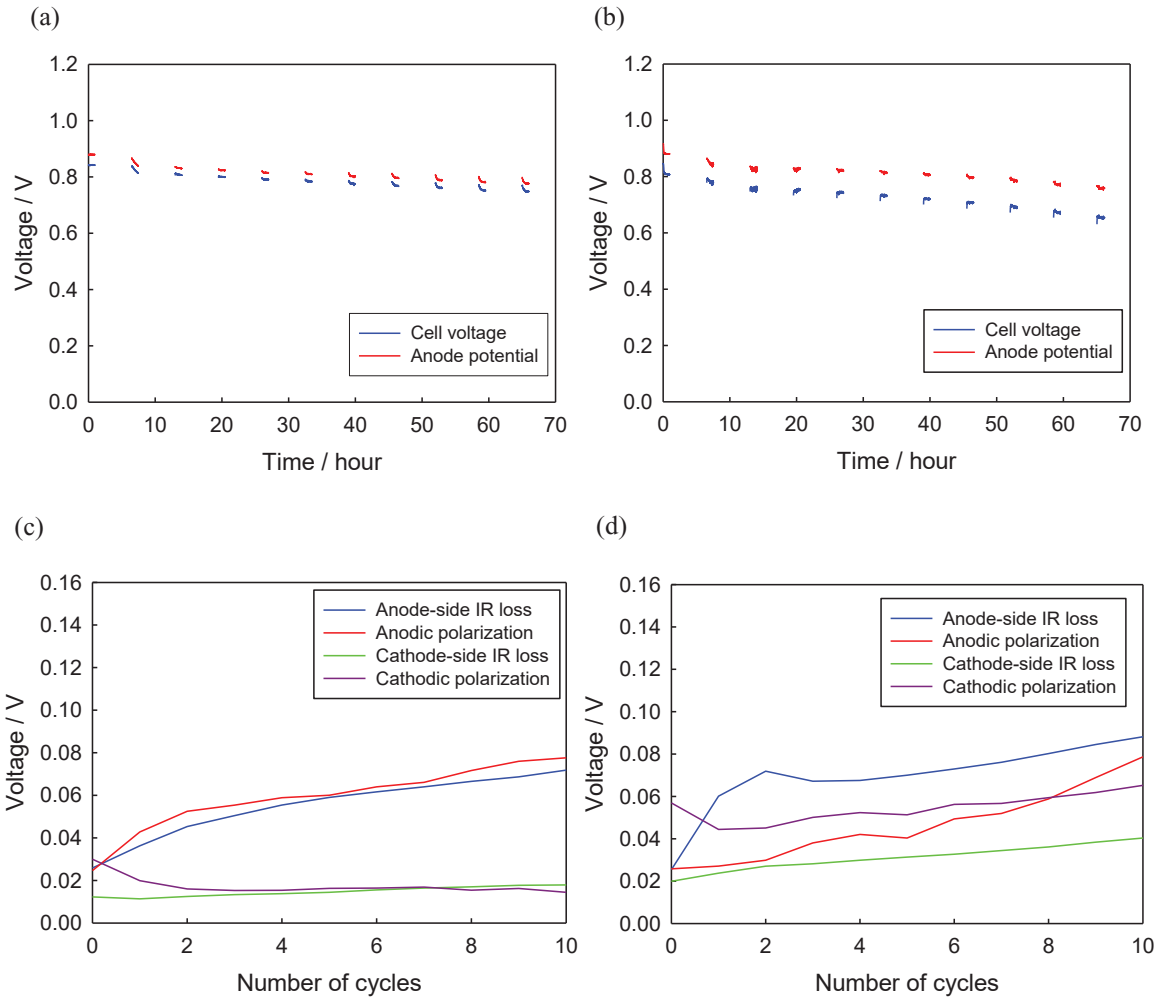

Figure 11. (a,b) Cell voltage, anode potential (vs. RE, in air), and (b,d) voltage losses (ohmic loss and non-ohmic polarization at the anode and the cathode), at 0.2 Acm^{-2} during a 10-cycle cool down durability test (cool down rate: 100°C h^{-1}, 50% pre-reformed CH_4-based fuel (a,c) without H_2S and (b,d) with 5 ppm H_2S).

The elemental distribution and connectivity of nickel and zirconia in the anode were analyzed quantitatively by 3-dimensional (3D) reconstructed FIB-SEM, just after the initial reduction treatment (Fig. 10c), and after the 74-cycle shutdown test (Fig. 10d). These two micrographs clearly indicate that Ni grains agglomerated and grew in size in the anode layer during the 74-cycle test. Furthermore, Fig. 10d shows elemental distribution, highlighting the isolated Ni grains in the anode layer, and showing that the continuous Ni networks were destroyed. Consequently, the anode-side IR loss increased significantly and the cell no longer generated significant power. This is in contrast to the test immediately after the initial reduction treatment (Fig. 10c) where isolation of the Ni grains is negligible.

These results indicate that slower cool down rates result in fuel-starvation and exposure to oxidizing atmosphere at lower temperatures for longer periods of time, leading to anode Ni oxidation. Furthermore, volume changes in Ni at the anode by repeated oxidation/reduction cycles further accelerate Ni agglomeration and grain growth.

Dependence on fuel species.— Electrochemical performance of the model cells tested using the shutdown protocol with the slowest cool down rate was further examined using three different fuel species; (i) 3%-humidified H_2, (ii) 50% pre-reformed CH_4, and (iii) H_2S-containing, 50% pre-reformed CH_4. Ten thermal cycles were performed for each test. The cell voltage and the anode potential for the cell with the 50% pre-reformed CH_4 fuel with and without H_2S are shown in Fig. 11. The degradation rates per 10 cycles are; (i) 11.6%, (ii) 10.9%, and (iii) 19.0%, respectively. There is no significant difference in degradation rate between (i) the 3% humidified H_2 and (ii) the 50% pre-reformed CH_4. However, the degradation rate for (iii) H_2S-containing 50% pre-reformed CH_4 was about twice as high, showing that sulfur has negative influence on cell durability in shutdown tests. Post-test EDX elemental mapping of the anode cross-section (near the anode-electrolyte interface) revealed an O/Ni ratio of 0.95 for the H_2S-containing fuel, clearly indicating that the anode Ni is oxidized and significantly agglomerated on the anode side, leading to such serious degradation.

It is already known that sulfur species adsorb onto the surface of Ni anode catalysts when H_2S is mixed into fuels,[19,20] resulting in both electrode and internal reforming reactions being deactivated. As a result, oxygen ions passing through the electrolyte contribute to oxidation of the anode Ni, rather than the electrode reactions necessary for fuel cell operation. In addition, in the case that internal reforming reactions ($CH_4 + H_2O \rightarrow 3H_2 + CO$) are deactivated, the water vapor concentration increases on the anode side because it is not consumed. Under such high-humidity conditions, Ni is more easily oxidized. Consequently, Ni oxidation is accelerated in the presence of sulfur impurities, leading to a decrease in both the electronic conductivity and the electrode activity, which correspond to higher ohmic and non-ohmic losses, respectively. This is probably the origin of the cell performance degradation.

Thermal / Fuel Cycle Degredation

The fuel supply was stopped during cooling in shutdown tests. Therefore, there are two possible contributions to acceleration of degradation; thermal cycling, or interruption of fuel supply. We therefore conducted durability tests both with / without thermal cycling, and with / without fuel supply interruption, in order to understand the influence of each contribution. The change in cell voltage, anode potential, and deconvoluted voltage losses are shown in Fig. 12.

Effect of thermal cycling.— A shutdown test was performed without interruption of the fuel supply. Fuel (3%-humidified H_2) was continuously supplied throughout the test in order to reveal only the effect of thermal cycling. Negligible degradation is observed (Fig. 12a), and the anodic polarization increases only slightly (Fig. 12c). One of the reasons for this small increase in anodic polarization may be agglomeration of Ni, accelerated by the thermal expansion mismatch between Ni and ScSZ.

Effect of fuel supply interruption.— A shutdown test was performed without thermal cycling. The temperature was maintained at 800°C, but the fuel supply was interrupted during the designated time periods of the shutdown protocol. Figure 12b shows that significant cell degradation occurs. Anode-side losses are predominant; in particular the anode-side ohmic loss (Fig. 12d), as with the other shutdown tests. From these results it is concluded that cell performance degradation in shutdown tests is mainly attributed to the redox cycling caused by interruption in fuel supply, rather than thermal cycling.

Additionally, the open circuit voltage (OCV) also indicates that the cell voltage significantly drops shortly after fuel supply interruption. It is known that Ni metal oxidizes at around 0.7 V, derived from the oxygen partial pressure at the phase boundary of Ni and NiO. The cell voltage fell below 0.6 V around 6 minutes after fuel interruption, oxidizing the Ni. After that the cell voltage drops to around 0 V, indicating that the oxygen partial pressure on the anode side matches that on the cathode side. In other words, no hydrogen was available on the anode side, such that the anode was exposed to oxidizing atmosphere for a longer time. Oxidation and agglomeration of anode Ni are promoted in this situation, leading to cell performance degradation. This degradation is suppressed if fuel is continuously supplied to keep the anode atmosphere under reducing conditions. These results also suggest that tubular or flat-tubular SOFCs (without the need for glass sealing) are more suited to practical residential applications.

Nickel Precipitation at the Electrolyte Grain Boundaries

Electrolyte fracture surfaces were observed after 250 cycles for the different durability tests. Ni particles were found at the grain boundaries of the electrolytes, especially near the anode. This phenomenon was most prominent after shutdown tests. For example, Fig. 13 shows the electrolyte fracture surface after a 250-cycle shutdown test utilizing 3%-humidified H_2. Table I compiles the experimental conditions in which Ni particles were precipitated in the electrolyte. This effect was more pronounced in more oxidizing atmosphere, with higher water vapor concentration, and at lower temperature. Figure 14 shows FESEM micrographs and EDX elemental mapping of the electrolyte

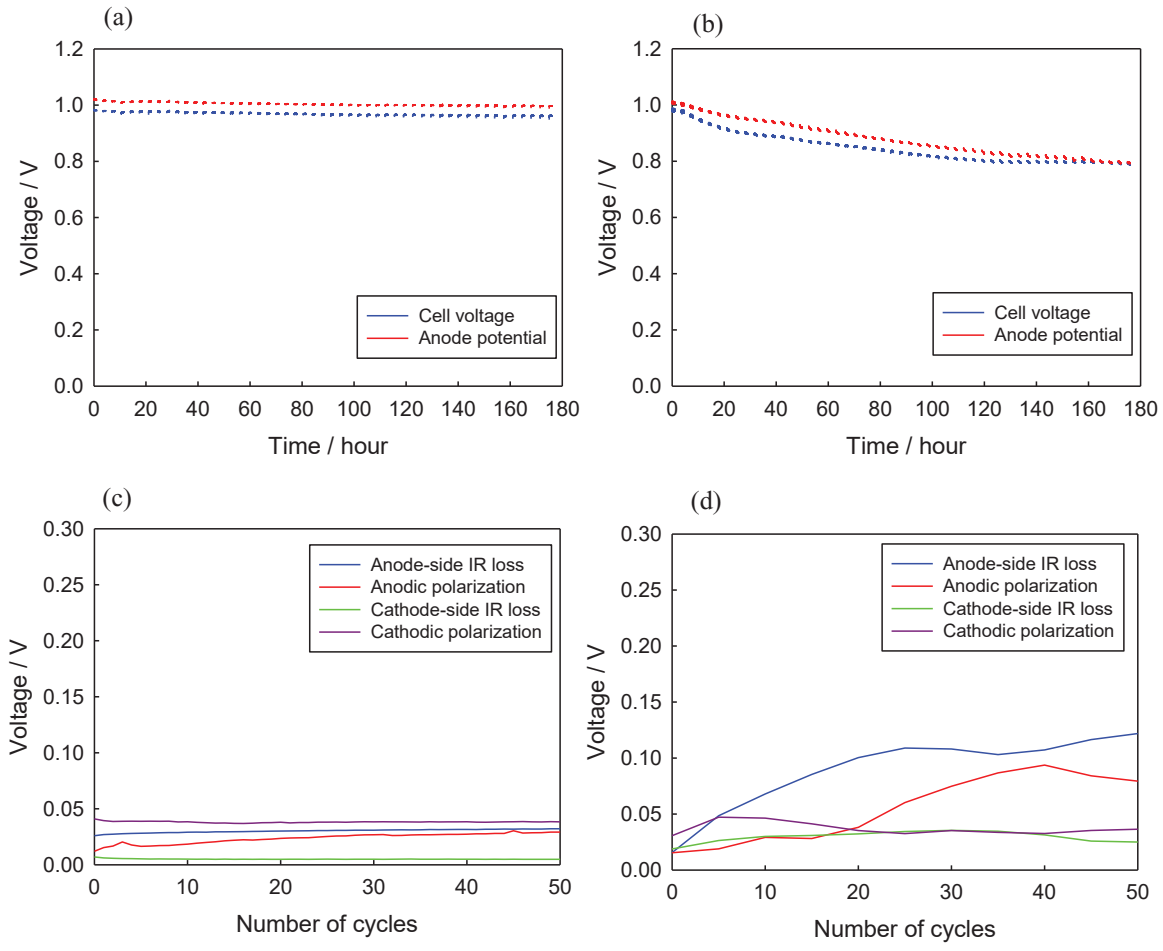

Figure 12. (a,b) Cell voltage and anode potential (vs. RE, in air), and (c,d) voltage losses (ohmic loss and non-ohmic polarization at both the anode and the cathode) at 0.2 Acm^{-2}, during 50-cycle shutdown durability tests (3%-humidified H_2 fuel). In (a,c) the fuel supply is maintained throughout the test. In (b,d) the temperature is kept constant throughout the test.

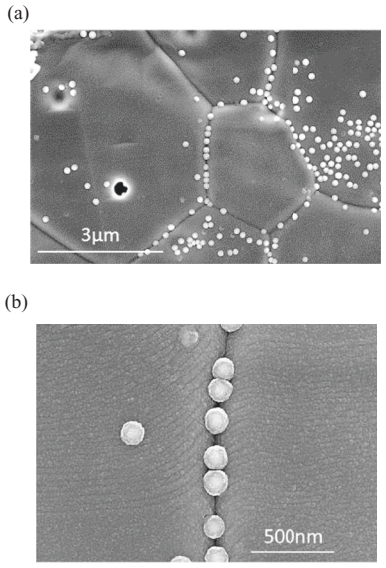

Figure 13. FESEM micrographs of the electrolyte fracture surface in the vicinity of the anode, after the 250-cycle shutdown durability tests (cool down rate: 400°C h^{-1}, 3%-humidified H_2 fuel).

fracture surface (a) before and (b) after the durability test. EDX analysis reveals that particles precipitated in the electrolyte are metallic Ni. Such Ni precipitation has also been observed in YSZ electrolytes.[21]

It should be noted that NiO dissolves in the electrolyte during high temperature sintering of the anodes in air, especially at grain boundaries.[22–24] Here, analysis of the electrolyte fracture surface after anode sintering confirms that NiO had already dissolved around the grain boundaries of the electrolyte during sintering, as shown in Fig. 14a. Based on the above results, the mechanisms of Ni particle precipitation in the electrolyte may be understood as follows:

(i) A small amount of NiO dissolves at the electrolyte grain boundaries during high-temperature sintering in air.
(ii) Metallic Ni precipitates at the grain boundaries upon reduction during cycling.
(iii) Some Ni particles remain at the grain boundaries during further oxidation cycles.
(iv) Ni particles at the grain boundary grow by absorbing precipitated metallic Ni during further reduction cycles.
(v) Ni particles grow by repeated oxidation/reduction cycles at the grain boundaries.
(vi) The growth of Ni particles halts when all of the dissolved Ni around the grain boundaries has been adsorbed onto the residual metallic Ni grains.

Through the above processes, precipitated Ni particles gradually grow, as shown in Figs. 13 and 14. Ni particle precipitation in the electrolyte can lead to a decrease in mechanical strength of the electrolyte, potentially leading to fracture during thermal cycling. Additionally,

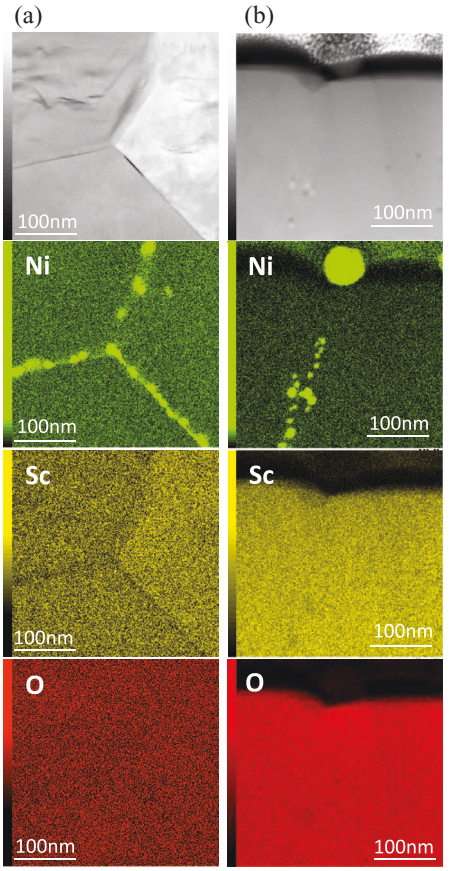

Figure 14. FESEM micrographs and EDX elemental mapping (Ni, Sc, and O) of the electrolyte fracture surface in the vicinity of the anode, after (a) the initial reduction treatment, and (b) the 250-cycle shutdown durability test (cool down rate: 400°C h^{-1}, 3%-humidified H_2 fuel).

dissolved NiO and precipitated metallic Ni particles may affect the electrolyte grain boundary resistivity by blocking ionic conduction.

Summary

The cycle durability of electrolyte-supported SOFCs was systematically investigated under realistic operating conditions, by varying the temperature and/or fuel supply. Three different protocols were used; hot standby, cold standby, and shutdown. The cell performance degraded during repeated cold standby and shutdown modes, whilst negligible degradation was observed in hot standby. As compiled in Fig. 15, degradation was significantly influenced by both the cool down rate (i.e., the period of time during cooling), and the presence of H_2S in the fuel feedstock. As summarized in Fig. 16, possible degradation mechanisms include; (i) Ni agglomeration; (ii) Ni oxidation (accelerated by the presence of H_2S); (iii) Ostwald ripening; (iv)

Table I. Experimental conditions for Ni particle precipitation along the zirconia electrolyte grain boundaries (++ precipitated, +: partially precipitated, –: not precipitated, N.A.: not analyzed).

	3%-humidified H_2			50% pre-reformed CH_4		50% pre-reformed $CH_4 + H_2S$	
	10 cycles	50 cycles	250 cycles	10 cycles	50 cycles	10 cycles	50 cycles
Shutdown (over 1 h)	+	++	++	++	++	++	++
Shutdown (over 2 h)	+	N.A.	++	++		++	
Shutdown (over 4 h)	+		++	++	N.A.	++	N.A.
Hot standby	–	–	–	++		++	
Cold standby	–	–	N.A.	–		–	

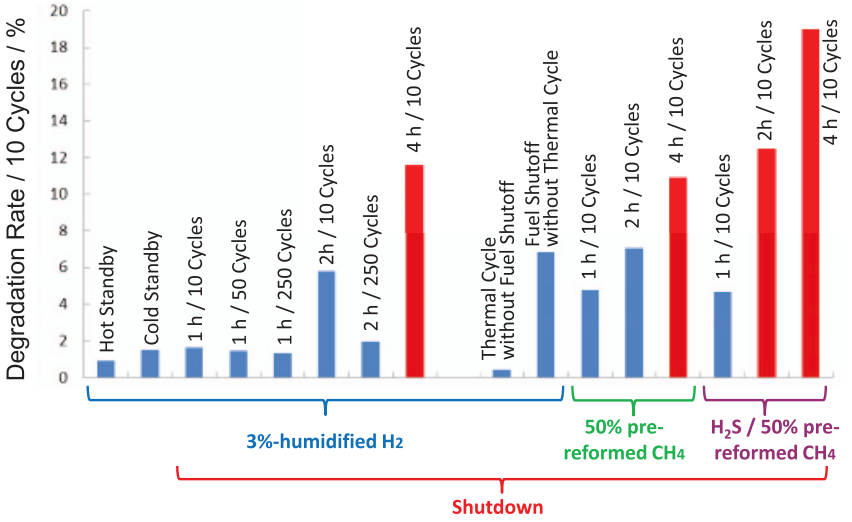

Figure 15. Average degradation rates per 10 cycles during durability tests with various different conditions.

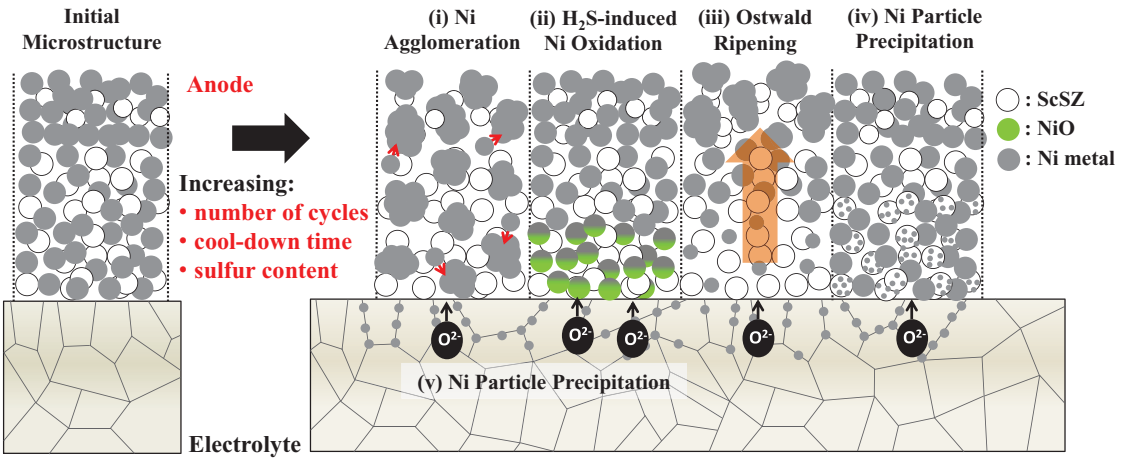

Figure 16. Schematic drawing of the degradation mechanisms occurring during cycle durability tests, including; (i) Ni agglomeration; (ii) Ni oxidation accelerated by H_2S; (iii) Ostwald ripening; (iv) Ni precipitation on anode zirconia grains; and (v) Ni precipitation at electrolyte grain boundaries.

Ni precipitation on anode zirconia grains; and (v) Ni precipitation at electrolyte grain boundaries. Other mechanisms such as mechanical degradation induced by thermal expansion mismatch may also occur.

The main origin of cell performance degradation is the interruption of fuel supply, which promotes Ni oxidation at the anode. In the case of sulfur poisoning, the water vapor concentration increased on the anode side, and Ni grains were thus easily oxidized (H_2S deactivates both electrode and internal reforming reactions). Ni oxidation may also be accelerated by insufficient sealing after thermal cycling. In addition, a decrease in the amount of Ni around the triple-phase boundary, and consequent Ni grain coarsening around the anode surface were identified, explained by the Ostwald ripening mechanism (via $Ni(OH)_2$ in the gas phase). Precipitation of Ni on the surface of zirconia particles, and at grain boundaries in the electrolyte was also newly identified. All these phenomena lead to a decrease in electrode activity and consequent cell performance degradation during cycling. Since this cycle-induced degradation seems to be a relatively complicated process, more detailed studies should be performed. Other operational parameters and conditions including cathodic and anodic overvoltage, cell components (including sealing materials), and their geometric structure may also affect degradation rates. We aim to address these issues in the near future.

Acknowledgment

The authors thank the New Energy and Industrial Technology Development Organization (NEDO) for supporting this study. We thank R. Rika Taniguchi for her FIB-SEM analysis, and Ayumi Zaitsu for her editorial support. The International Institute for Carbon-Neutral Energy Research is supported by World Premier International Research Center Initiative (WPI), MEXT, Japan.

References

1. W. Bujalski, J. Paragreen, G. Reade, S. Pyke, and K. Kendall, *J. Power Sources*, **157**, 745 (2006).
2. W. Bujalski, C. M. Dikwal, and K. Kendall, *J. Power Sources*, **171**, 96 (2007).
3. Y. Guan, Y. Gong, W. Li, J. Gelb, L. Zhang, G. Liu, X. Zhang, X. Song, C. Xia, Y. Xiong, H. Wang, Z. Wu, and Y. Tian, *J. Power Sources*, **196**, 10601 (2011).
4. N. Takagi, N. Shikazono, and N. Kasagi, *Proc. JSME Annual Meeting*, Morioka Japan, The Japan Society of Mechanical Engineers, pp. 119 (2009).
5. T. Werber, *Solid State Ionics*, **42**, 205 (1990).
6. D. Waldbilling, A. Wood, and D. G. Ivey, *J. Power Sources*, **145**, 206 (2005).
7. B. Liu, Y. Zhang, B. Tu, Y. Dong, and M. Cheng, *J. Power Sources*, **165**, 114 (2007).
8. K. Fujita, T. Somekawa, K. Horiuchi, and Y. Matsuzaki, *J. Power Sources*, **193**, 130 (2009).
9. J. Laurencin, G. Delette, O. Sicardy, S. Rosini, and F. Lefebvre-Joud, *J. Power Sources*, **195**, 2747 (2010).
10. Q. Jeangros, A. Faes, J. B. Wagner, T. W. Hansen, U. Aschauer, J. van Herle, A. Hessler-Wyser, and R. E. Duni-Borkowski, *Acta Materialia*, **58**, 4578 (2010).
11. H. Sumi, R. Kishida, J. Kim, H. Muroyama, T. Matsui, and K. Eguchi, *J. Electrochem. Soc.*, **157**(12), B1747 (2010).
12. M. H. Pihlatie, A. Kaiser, M. Mogensen, and M. Chen, *Solid State Ionics*, **189**, 82 (2011).
13. L. Holzer, B. Iwanschitz, Th. Hocker, B. Munch, M. Preatat, D. Wiedenmann, U. Vogt, P. Holtappels, J. Sfeir, A. Mai, and T. Graule, *J. Power Sources*, **196**, 1279 (2011).

14. L. Holzer, B. Iwanschitz, T. Hocker, L. Keller, O. Pecgo, G. Sartoris, P. Gasser, and B. Muench, *J. Power Sources*, **242**, 179 (2013).
15. K. Sasaki, S. Adachi, K. Haga, M. Uchikawa, J. Yamamoto, A. Iyoshi, J. T. Chou, Y. Shiratori, and K. Itoh, *ECS Trans.*, **7**, 1675 (2007).
16. S. B. Adler, *J. Electrochem. Soc.*, **149**(5), E166 (2002).
17. T. Yoshizumi, S. Taniguchi, Y. Shiratori, and K. Sasaki, *J. Electrochem. Soc.*, **159**(11), F693 (2012).
18. K. Haga, Y. Shiratori, K. Ito, and K. Sasaki, *J. Electrochem. Soc.*, **155**, B1233 (2008).
19. Y. Matsuzaki and I. Yoshida, *Solid State Ionics*, **132**, 261 (2000).
20. K. Sasaki, K. Susuki, A. Iyoshi, M. Uchiyama, N. Imamura, H. Kusaba, Y. Teraoka, H. Fuchino, K. Tsujimoto, Y. Uchida, and N. Jingo, *J. Electrochem. Soc.*, **153**, A2023 (2006).
21. M. Hanasaki and K. Sasaki, unpublished results.
22. W. G. Coors, J. R. O'Brien, and J. T. White, *Solid State Ionics*, **180**, 246 (2009).
23. H. Kishimoto, N. Sakai, T. Horita, K. Yamaji, Y. P. Xiong, M. E. Brito, and H. Yokokawa, *Solid State Ionics*, **179**, 2037 (2008).
24. H. Kishimoto, K. Yashiro, T. Shimonosono, M. E. Brito, K. Yamaji, T. Horita, H. Yokokawa, and J. Mizusaki, *Electrochimica Acta*, **82**, 263 (2012).